



# Effects of Annealing Treatment on Corrosion Resistance of Arc Sprayed Aluminum Coating

Muhammad Abaid Ashraf<sup>1</sup> · Nisar Ahmed<sup>1</sup> · Zuhair Subhani Khan<sup>1</sup> ·  
Muhammad Azhar Iqbal<sup>1</sup> · Aamir Naseem Satti<sup>1</sup> · Ameer Farooq<sup>2</sup>

Submitted: 11 June 2021 / in revised form: 26 March 2022 / Accepted: 2 May 2022 / Published online: 13 May 2022  
© ASM International 2022

**Abstract** Arc sprayed aluminum (Al) coatings are used as protection for steel substrates due to their corrosion resistance and cost-effectiveness. This research focuses on the influence of annealing on morphology, chemical composition, and corrosion resistance of arc sprayed Al coatings. The coatings were sprayed on mild steel substrate and annealed at various temperatures. The oxide content in the coatings and elemental diffusion between coating and substrate increased with the increase in annealing temperature. Moreover, the grain size of the coatings enlarged with increasing the annealing temperature up to 600 °C and decreased after annealing at 700 °C. The electrochemical studies suggested that the corrosion resistance of the coatings annealed at 500 and 600 °C was decreased compared to that of the as-sprayed coating. The coating annealed at 700 °C showed the lowest corrosion current density ( $1.504 \mu\text{A}/\text{cm}^2$ ), noble corrosion potential ( $-0.59 \text{ V}$  versus Ag/AgCl), and higher charge transfer resistance ( $511.76 \text{ k}\Omega\text{cm}^2$ ), indicating the highest corrosion resistance caused by lower percentage of porosity, finer grain size and formation of corrosion resistant  $\text{Al}_2\text{O}_3$  on its surface.

**Keywords** aluminum · annealing · arc spraying · corrosion · grain size

## Introduction

Plain carbon steels are extensively used in many applications due to their superior mechanical characteristics, versatility, and economic benefits. Their atmospheric corrosion is a big concern in harsh conditions such as seashore environments that limit their applications (Ref 1, 2). The degradation of steel is a continuous process, but it can be slowed down by various protective schemes such as galvanized coatings, corrosion inhibitors, cathodic protection, and thermal spray coatings (Ref 3–5). Thermal spraying is an effective way to combat degradation because of its convenience and minimum drawbacks (Ref 6). Thermal spray coatings are deposited when feedstock material in powder or wire form is melted by heat and accelerated towards the substrate to deposit a material layer. The coatings can offer corrosion protection as well as a wear barrier to the substrates (Ref 7).

There are various methods to deposit thermally sprayed protective coatings, including flame, atmospheric plasma, wire arc, and high-velocity oxy-fuel spray process (Ref 8–10). Wire arc spraying is an extensively used process to deposit anti-corrosion coatings because of its suitability, high deposition rates, and low operating costs (Ref 11, 12). This process uses electrically conductive and ductile wires as feedstock material. The material melts when two oppositely charged wires are fed together in such a way that an arc occurs at their meeting point. Subsequently, the melted material is atomized and accelerated in the direction of the substrate by a stream of pressurized air. The melted material droplets solidify immediately after colliding with the substrate and form a thick coating (Ref 13). Various metals are being deposited by the wire arc spraying process, such as zinc, aluminum, nickel, and their alloys. It is

✉ Muhammad Abaid Ashraf  
abaid.ashraf@yahoo.com

<sup>1</sup> U.S.-Pakistan Center for Advanced Studies in Energy, National University of Sciences and Technology, Islamabad 44000, Pakistan

<sup>2</sup> Corrosion Control Research Cell, Institute of Metallurgy and Materials Engineering, University of the Punjab, Lahore 54590, Pakistan

possible to deposit alloy coatings by this technique using dissimilar metal wires (Ref 14, 15).

Aluminum coatings deposited by arc spraying technique are commonly used to provide protection to steel structures, pipelines, and naval architecture in corrosive atmospheres, including exhaust gases reaching high temperatures (Ref 16–18). These coatings provide a barrier against the environment as well as they are anodic to the carbon steel substrates in seawater, which abolish the need for a complete barrier between atmosphere and substrate because they sacrificially protect the steel surface (Ref 19).

Annealing of arc spray coatings can significantly affect their properties by changing their microstructures. Ly et al. suggested that annealing treatment can improve the microhardness of arc sprayed Al-NiCr20 duplex coating by reducing its porosity (Ref 20). Guo et al. found that the annealing of Fe-based amorphous coatings can significantly improve their oxidation resistance by eliminating inherent discontinuities such as pores and cracks (Ref 21). Similarly, Lin et al. investigated the fracture toughness and erosion behavior of FeNiCrBSiNbW coatings after annealing and found that both properties deteriorate with increase in the annealing temperature (Ref 22). The annealing treatment of arc sprayed aluminum coating can increase its bonding strength caused by the interdiffusion of aluminum and other metal atoms (Ref 23). It oxidizes at high temperatures and forms an aluminum oxide film on its surface, which provides a barrier against oxygen diffusion (Ref 24). Zhou et al. studied the impact of annealing on the composition, element diffusion, and microstructure of arc sprayed aluminum coating and found that it adopts nearly flawless structure after annealing at 700 °C and/or 800 °C (Ref 25). However, the effect of annealing on its corrosion behavior has not been studied yet.

In this work, the aluminum coating was sprayed onto the mild steel substrate via wire arc spraying process followed by annealing at different temperatures. The effect of annealing temperatures on the chemical composition, morphology, and corrosion resistance of the coating was explored.

## Experimental Procedure

Commercially available mild steel (Table 1) was used as a substrate. Before the coating process, substrates were grit blasted by a sandblasting machine (SX-80F, Guangzhou

**Table 1** Chemical composition of mild steel substrate

Element	C	Si	Mn	P	S	Fe
wt. %	0.21	0.16	0.10	0.016	0.008	Bal.

Sanxin Metal Co., Guangzhou, China) using Al<sub>2</sub>O<sub>3</sub> particles at 5~6 bar air pressure to enhance the adhesion of coating with substrate by increasing substrate roughness and removing the oxides on its surface. The final average surface roughness value (Ra) of the mild steel substrate was 8.6 ± 1.5 μm. Afterward, the substrates were cleaned with acetone, followed by drying in an oven. The substrates were then arc sprayed using twin wires ( $\phi = 2$  mm) of commercially pure aluminum (99%) by wire arc spray system (SX-400, Guangzhou Sanxin Metal Co., Guangzhou, China). The dimension of the sprayed samples was 50 × 50 × 1 mm. The deposition parameters used for the arc spraying process are given in Table 2.

The coating samples were annealed at 500, 600 and 700 °C in a box furnace for 2 hours. For each sample, the temperature was raised from room temperature to desired annealing temperature with the ramp up of 10 °C/min. After completion, the heating was stopped, and the samples were cooled inside the furnace.

The cross-sections of the coating samples were ground with 1500 grit sandpaper followed by polishing using a 1-μm diamond paste to prepare them for the cross-sectional analysis. The as-sprayed surface morphologies and polished cross-sections of coatings were observed by a scanning electron microscope (SEM) (VEGA3, TESCAN, Brno, Czech Republic) operated at 20 kV. The elemental compositions of the coatings at the surface and interface were analyzed using an energy dispersive x-ray spectroscopy (EDS) (INCA X-act, Oxford Instruments, Abingdon, United Kingdom) system that was also operated at the accelerating voltage of 20 kV. The porosity of every coating sample was measured on five SEM cross-sectional micrographs at the magnification of 4 kx using an image analysis software (ImageJ), and its average value was considered as the porosity for the whole sample. X-ray diffraction (XRD) (D8 Advance, Bruker, Massachusetts, US) analysis was performed using Cu K $\alpha$  radiation ( $\lambda = 0.15406$  nm) generated at 40 kV and 30 mA to analyze the phase compositions of the coatings. The grain size of the coatings was determined using the Scherrer method (Ref 26)

**Table 2** Wire arc spray process parameters for aluminum coating

Spray parameters	Values
Standoff distance	100 mm
Compressed air pressure	5~6 bar
Voltage	42.5 V
Current	150 A
Spray angle	90°

$$L = \frac{k\lambda}{\beta \cos \theta} \quad (\text{Eq 1})$$

Here  $L$  indicates crystal size,  $k=0.89$  is the shape factor,  $\lambda=0.15403$  nm is the wavelength of x-ray source (Cu  $K\alpha$ ),  $\beta$  represents full width at half maximum, and  $\theta$  is diffraction angle.

Corrosion properties of all the coatings (as-sprayed and annealed) were assessed by potentiodynamic polarization (PDP) and electrochemical impedance spectroscopy (EIS) tests in a 3.5 wt.% NaCl solution to simulate the corrosion in the saline environment. These tests were accomplished by a three-electrode cell where the coating sample was used as working electrode, Ag/AgCl (sat. KCl) acted as reference electrode, and platinum wire as counter electrode. Prior to electrochemical tests, the coating samples were submerged in the electrolyte solution for 1 hour to stabilize the potential. An electrochemical workstation (CHI 660, CH Instruments Inc., Austin, US) was used to carry out electrochemical tests at room temperature. The PDP studies were carried out by scanning the potential from  $-1.6$  to  $+0.3$  V versus OCP at a scan rate of 1 mV/s. The EIS studies were performed by applying the AC amplitude potential of 10 mV between 100 kHz and 0.01 Hz frequency interval.

## Results and Discussion

### Characterization of Coatings

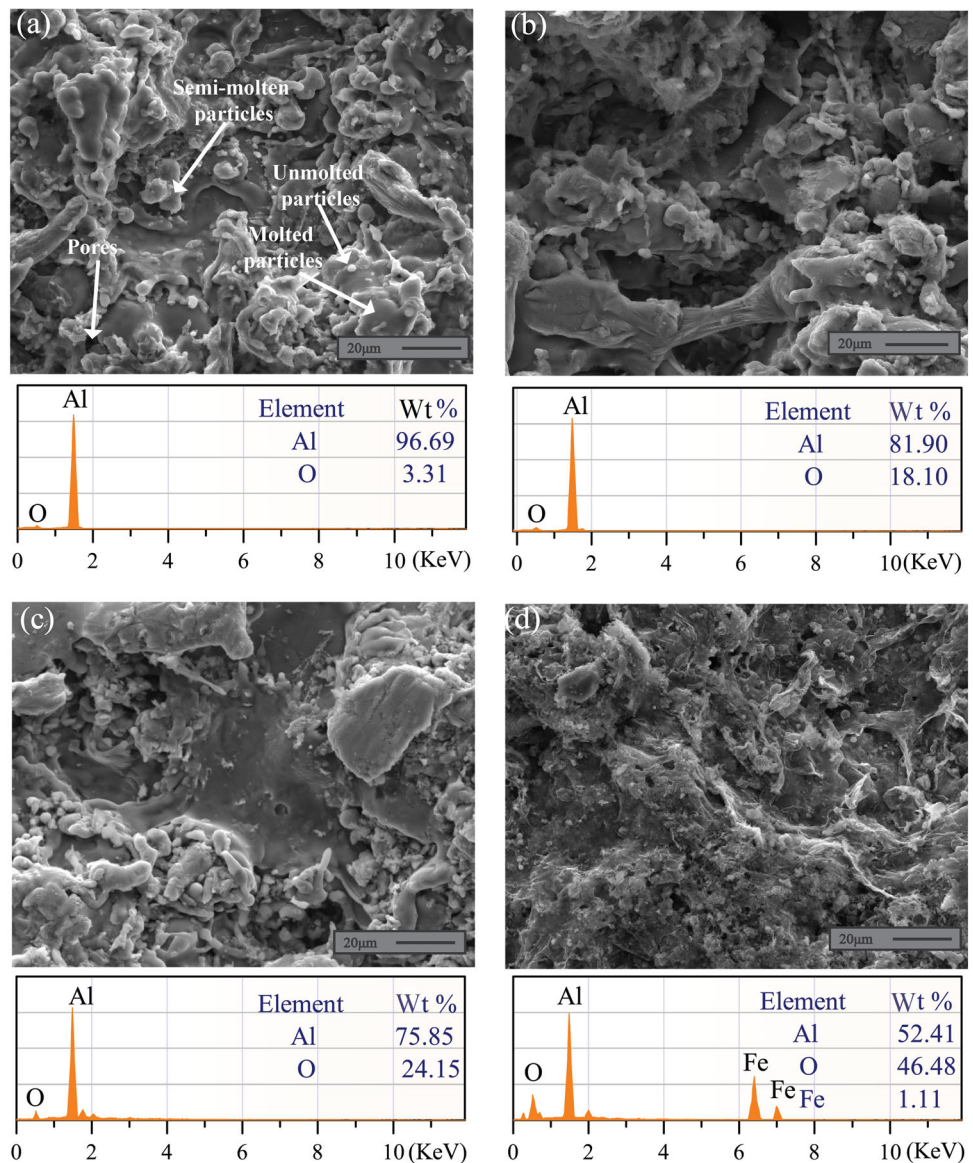
Figure 1 shows the SEM micrographs of the as-sprayed and annealed Al coatings. Molten, semi-molten, and un-melted particles are visible on as-sprayed (Fig. 1a) coating, which leads to very rough surface morphology. The coating surface exhibited a splat zone consisting of an irregular plate-like morphology, and pores. The main reason for the porosity is the entrapment of gases during the spraying process (Ref 27). The abovementioned features are inherent properties of thermally sprayed coatings, and they are unavoidable. It is apparent that many small droplets that were observed on as-sprayed coatings gradually disappeared after annealing (Fig. 1b, c). Moreover, the coating displayed a different microstructure after annealing at 700 °C. This occurred because the melting point of aluminum is 660.54 °C, and the coating became liquid above this temperature and converted into a composite coating. As the temperature of the sample dropped below the melting point of aluminum, solidification occurred, and a new structure formed (Ref 28).

Table 3 presents the EDS analysis of all coating surfaces. Aluminum was the primary element in the as-sprayed coating, but it also consisted of 3.31 wt.% of

oxygen. The oxygen comes during the coating process due to the oxidation of inflight molten material particles and the oxidation of the coating surface after spraying. Generally, the oxygen content in wire arc sprayed coatings is between 2 and 8%, which can be further reduced by varying the spraying parameters and conditions (Ref 14). The oxygen content in the as-sprayed aluminum coating was in the typical range. However, it increased significantly to 18.10 and 24.15% in the coatings when the annealing temperature reached 500 and 600 °C, respectively. The oxygen content was directly proportional to the annealing temperature and increased due to the oxidation of aluminum in the air during the annealing process. The oxygen was highest (46.48%) in the coating after annealing at 700 °C. Additionally, a small amount of Fe was also detected on its surface, which suggested that Fe was diffused to the surface of the coating from the substrate after annealing at 700 °C (Ref 29). Since the accelerating voltage for the EDS analysis was 20 kV, the excitation volume within the material would have been large, indicating that the specific surface of the particles also played a big role in the measurement of oxygen in the coatings. Moreover, the EDS analysis is not very efficient in determining the elemental composition and detecting the light elements, including oxygen, hence the compositions of the coatings were also determined by the XRD analysis.

SEM cross-sectional micrographs of all coatings are given in Fig. 2. The thickness of coatings after deposition was approximately 180  $\mu\text{m}$ . A well-bounded coating having uniform thickness was observed without any irregular interface in the cross-sectional image (Fig. 2a). Moreover, it did not exhibit the typical laminar feature of thermally sprayed coatings, and the main reason behind this phenomenon is the low melting point of aluminum that enabled the depositing melted particles to homogenize during the coating process (Ref 30). The coatings became more compact as the annealing temperature increased, and the interface after annealing was less distinctive compared to as-sprayed coating. The diffusion layers were observed in the coatings when annealed at 500 and 600 °C (below the melting point of aluminum), as shown in Fig. 2(b) and (c), which is due to the diffusion of Fe atoms towards the coating (Ref 31). After annealing at 700 °C, the coating appeared without any big pores and looked more like a bulk material, as shown in Fig. 2(d). There was no definite diffusion layer, but the whole coating seemed a diffusion zone. The EDS analysis of the whole coating area indicated the co-existence of Al and Fe, which suggested that the Fe had diffused into the whole coating (Table 4). Fig 2(e) and (f) present the elemental mapping of the coating after annealing at 700 °C, indicating the interdiffusion of Al and Fe during the annealing process. The porosity in the as-sprayed coating was approximately  $1.63 \pm 0.12\%$ , and it

**Fig. 1** SEM micrographs of as-sprayed and annealed Al coatings (a) as-sprayed (b) 500 °C (c) 600 °C (d) 700 °C



**Table 3** EDS analysis of all coatings (wt. %)

Sample ID	Al	O	Fe
As-sprayed	96.69	3.31	....
Annealed at 500 °C	81.90	18.10	....
Annealed at 600 °C	75.85	24.15	....
Annealed at 700 °C	52.41	46.48	1.11

significantly decreased to  $0.48 \pm 0.14\%$ ,  $0.21 \pm 0.09\%$ , and  $0.1 \pm 0.03\%$  after annealing at 500, 600 and 700 °C, respectively. The reduction in porosity of the coatings with the rise in annealing temperature is expected to enhance their barrier properties by reducing the diffusion pathways and ultimately increase their corrosion resistance.

The x-ray diffraction spectrums of all coatings are given in Fig. 3(a). The as-sprayed coating primarily consisted of a pure aluminum phase. The maximum diffraction was at  $38.5^\circ$  corresponding to the crystal face (111), and other diffraction peaks were at  $44.7^\circ$ ,  $65.1^\circ$ ,  $78.2^\circ$ ,  $82.4^\circ$  confirming (200), (220), (311), and (222) crystal faces. The structure of aluminum coating remained the same even after annealing at 600 °C. Besides aluminum, no other peaks were detected on the surface of the coatings, which was due to the low concentrations of oxides. After annealing at 700 °C, significant changes occurred in the chemical structure of the coating, and two additional phases of  $Fe_2O_3$  and  $Al_2O_3$  were identified. The magnified image of the characteristic peaks of all coatings is shown in Fig 3(b). This figure indicates the induction of compressive

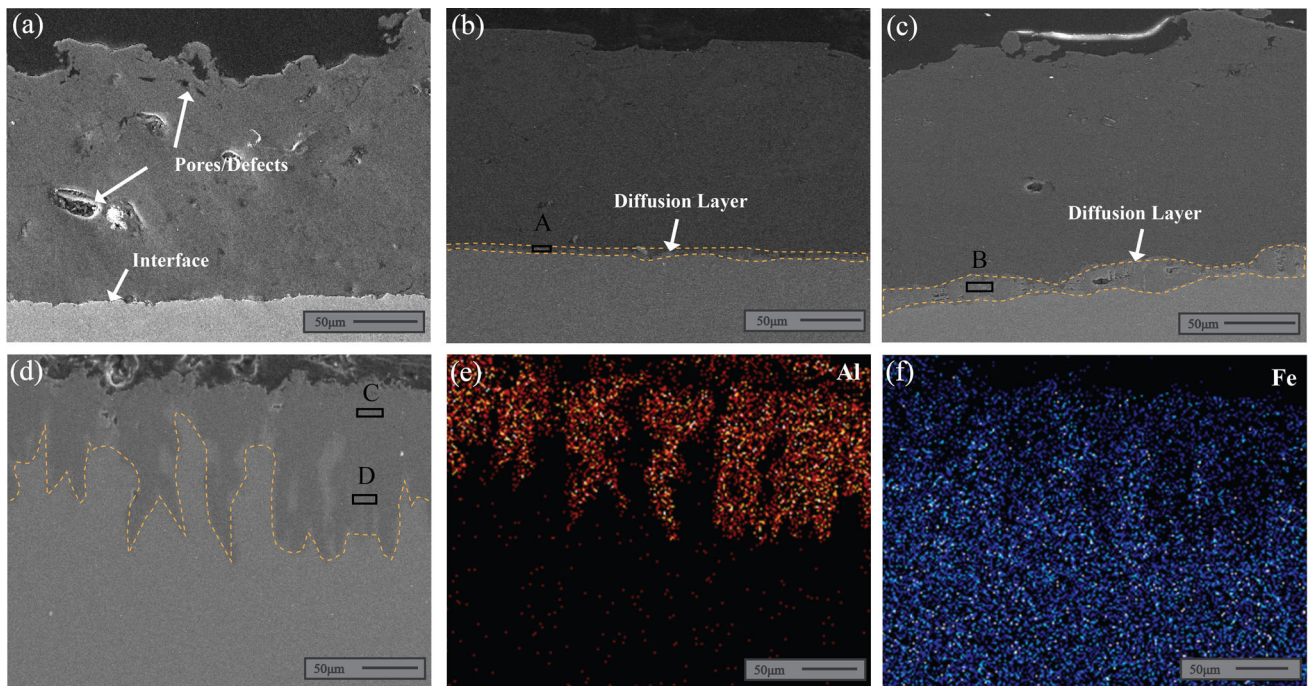


**Fig. 2** Cross-sectional images of as-sprayed and annealed Al coatings (a) as-sprayed; (b) 500 °C; (c) 600 °C; (d) 700 °C, elemental mapping of coating annealed at 700 °C indicating; (e) Al; (f) Fe

**Table 4** EDS Analysis of Points in Fig. 2 (wt. %)

EDS Points	Al	Fe
A	55.35	45.65
B	47.78	52.22
C	52.05	47.95
D	54.61	45.39

stresses in the coatings with the increase in annealing temperature until 600 °C.

The grain sizes of all coatings are illustrated in Fig. 3(c). The grain size increased with an increase in annealing temperature up to 600 °C. However, a significant reduction in crystallite size was observed when the annealing temperature was raised to 700 °C. The smaller grain size in the coating after annealing at 700 °C can be associated with the recrystallization of aluminum above its melting point as well as the smaller grain size of  $\text{Al}_2\text{O}_3$  (Ref 32). The  $\text{Al}_2\text{O}_3$  was formed on the surface of the coating as indicated by the XRD analysis. Alumina exhibits a smaller grain size compared to commercially pure aluminum (Ref 33).

### Electrochemical Tests

Figure 4 illustrates the potentiodynamic polarization (PDP) curves of all coatings. The electrochemical parameters, including corrosion potential ( $E_{\text{corr}}$ ), corrosion current density ( $i_{\text{corr}}$ ), and corrosion rate, were measured from each curve by the Tafel extrapolation method, and their values

are presented in Table 5. The PDP curve shows two branches, anodic and cathodic. The anodic branch formed when the electrode potential shifted from its open circuit potential to high polarized potential, and it shows the dissolution characteristics of the electrode. Whereas the cathodic branch formed when the electrode potential shifted from its open circuit potential to low polarized potential, and shows the reduction characteristics of the electrode. During Tafel extrapolating, the linear fitting of the anodic and cathodic branches results in an intersection point. This intersection point corresponds to  $E_{\text{corr}}$  and  $i_{\text{corr}}$  values along potential and current density axes, respectively. The  $E_{\text{corr}}$  is a thermodynamic variable that reflects the active or noble behavior of the samples while  $i_{\text{corr}}$  is a kinetic variable during the corrosion/dissolution process. According to Faraday's law,  $i_{\text{corr}}$  is related to corrosion rate (Ref 34).

The  $E_{\text{corr}}$  value of as-sprayed coating was found to be  $-1.01$  V versus Ag/AgCl which was more active compared to the underlying substrate (mild steel) that has  $\sim -0.33$  V versus Ag/AgCl in the same saline environment. The  $E_{\text{corr}}$  also reflects the sacrificial behavior of the coating as supported by the previous researchers (Ref 35). After annealing at 500 and 600 °C, a negative shift in the  $E_{\text{corr}}$  values was observed, and they were both recorded at approximately the same value of  $-1.05$  V versus Ag/AgCl. The annealing treatment at 500 and 600 °C reduces the porosity in the coatings, but it coarser their grain size,

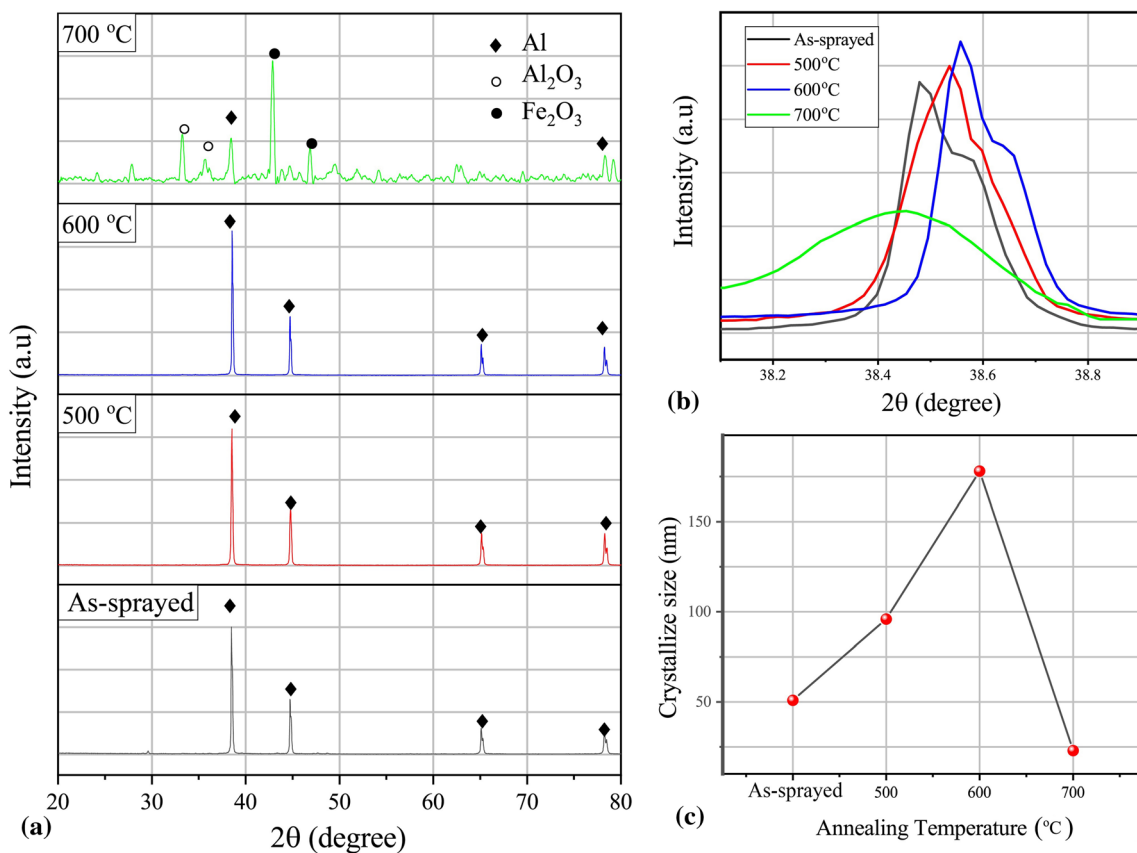


**Fig. 3** (a) XRD pattern of Al coatings before and after annealing, (b) Magnified image of characteristic peaks of all coatings, (c) Crystallite size of Al coatings before and after annealing

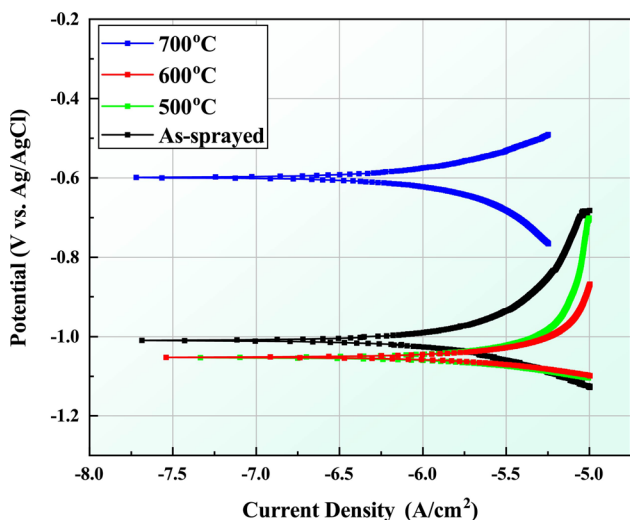


**Fig. 4** Potentiodynamic polarization (PDP) curves of all coating samples

which results in their active behavior. The  $E_{corr}$  of the coating shifted to a relatively positive value ( $-0.59$  V versus Ag/AgCl) compared to all coatings after annealing at  $700$  °C. Generally, a less negative value of  $E_{corr}$  represents a noble behavior in the aggressive saline environment

(Ref 36). The less negative potential of the coating annealed at  $700$  °C can be very significant in a saline environment. Because during the operation, if the coating gets damaged by any means, it will have less chance of galvanic corrosion compared to the other coatings because of the smaller potential difference between the coating and substrate. The  $i_{corr}$  value of the as-sprayed coating was  $2.40 \mu A/cm^2$ , and it increased to  $7.24$  and  $9.60 \mu A/cm^2$  after annealing at  $500$  and  $600$  °C, respectively. The coating exhibited the lowest  $i_{corr}$  value of  $1.50 \mu A/cm^2$  after annealing at  $700$  °C. The lower magnitude of  $i_{corr}$  value indicates a lower corrosion rate and higher corrosion resistance (Ref 37). The polarization resistance ( $R_p$ ) is the direct indicator of corrosion resistance, and it can be calculated by the Stern-Geary equation as illustrated in Eq. 2 (Ref 38).

$$R_p = \frac{b_a b_c}{2.303 i_{corr} (b_a + b_c)} \tag{Eq 2}$$

Here,  $b_a$  and  $b_c$  are the anodic and cathodic slope constant, respectively, in mV/decade,  $i_{corr}$  is the corrosion current density in  $\mu A/cm^2$ , and  $R_p$  is the polarization resistance in  $k\Omega \cdot cm^2$ .

**Table 5** The electrochemical parameters for as-sprayed and annealed Al coatings

Sample id	$E_{\text{corr}}$ , V vs. Ag/AgCl	$i_{\text{corr}}$ , $\mu\text{A}/\text{cm}^2$	Corrosion rate, mpy	$R_p$ , $\text{k}\Omega\cdot\text{cm}^2$
As-sprayed	− 1.01	2.40	0.60	11.30
Annealed at 500 °C	− 1.05	7.24	2.07	3.74
Annealed at 600 °C	− 1.05	9.60	3.17	2.83
Annealed at 700 °C	− 0.59	1.50	0.43	18.09

From the kinetic parameters, the polarization resistance of all the coatings was in the order: 700 °C > as-sprayed > 500 °C > 600 °C (Table 5). The corrosion resistance of the coatings depends on various factors such as grain size, pores, and chemical composition (Ref 39). The large grain size suggests the increase in the distance of the protective oxide nuclei on the grain boundary, and more time is needed to form continuous oxide scales (Ref 40). Hence, it can be determined that coarsening of grain size was the main factor for reduced corrosion resistance of coatings after annealing at 500 and 600 °C. The increase in corrosion resistance of the coating annealed at 700 °C can be associated with its finer grain size, compact microstructure, and presence of oxides such as alumina (Ref 21). The presence of alumina layer provides a barrier to reduce the oxygen diffusion inside the coating and protect it from further degradation (Ref 41).

The impedance spectra of all coating samples at different immersion times (1, 200 and 1000 hrs) are shown in Fig. 5. The electrochemical mechanisms of all the coatings were modeled by the equivalent electrical circuit (EEC) models (Fig. 6a, b) to simulate the EIS data. The EEC models consist of electrolyte solution resistance ( $R_s$ ), charge transfer resistance ( $R_{ct}$ ), double layer capacitance ( $Q_{dl}$ ), and diffusion variable Warburg impedance ( $W$ ). Generally, the constant phase element replaces the ideal capacitor due to the non-uniformity of dielectric characteristics of the coating and charge relaxation in the double layer (Ref 42). The results obtained after fitting the EIS data into EEC models are illustrated in Table 6. The non-ideal double layer capacitance can be calculated by the following formula (Ref 43).

$$Q_{dl} = \frac{1}{(2\pi f)^n Z''}$$

where  $Q_{dl}$  is the non-ideal double layer capacitance in  $\mu\text{F}/\text{cm}^2$ , 'f' is the frequency in Hz, 'n' is the charge relaxation coefficient, and  $Z''$  is the imaginary component of the impedance in  $\Omega\cdot\text{cm}^2$  (Ref 43).

The Nyquist plot of the as-sprayed coating (Fig 5a) shows the diffusion behavior after one hour of the immersion but after 200 hours of immersion, the electrolyte completely homogenized with the coating and formed a uniform double layer as shown in Fig. 6(a). The ECC model fitted on the coating after 1 hr immersion is shown

in Fig 6(a), while the ECC model fitted on the coating after 200 and 1000 hrs immersion is shown in Fig 6(b). The  $R_{ct}$  value of the as-sprayed coating was  $13.47 \text{ k}\Omega\cdot\text{cm}^2$ , and it gradually increased to 17.03 and  $408.51 \text{ k}\Omega\cdot\text{cm}^2$  after 1, 200, and 1000 hrs of immersion, respectively. The increase in the  $R_{ct}$  after increasing the immersion time is due to the formation of corrosion products on the surface of the coating. The coating was sacrificial in nature, so it reacted with the  $\text{Cl}^-$  ions in the electrolyte and formed corrosion products on its surface. The corrosion products don't show the diffusion behavior instead act as a barrier for further dissolution of the coatings. However, the  $R_{ct}$  value of the coating annealed at 500 °C decreased and it was recorded as 5.59, 11.87, and  $410.23 \text{ k}\Omega\cdot\text{cm}^2$  after 1, 200, and 1000 hrs of immersion, respectively. It further decreased in case of the coating annealed at 600 °C. In case of the coating annealed at 700 °C, the  $R_{ct}$  value increased from 20.44 to 33.46 and  $511.76 \text{ k}\Omega\cdot\text{cm}^2$  by increasing the immersion time from 1 hr to 200 hrs and 1000 hrs, respectively. The higher  $R_{ct}$  value indicates a lower dissolution rate and higher corrosion resistance (Ref 44). The  $Q_{dl}$  value of the coatings increased with the annealing temperature, apart from the annealing temperature of 700 °C, where it decreased. The lower value of  $Q_{dl}$  implies a thicker protective film and vice versa (Ref 45).

The diffusion mechanism in the arc sprayed Al coating has been reported by researchers in the past as well (Ref 46). Actually, the porous or heterogeneous surface morphology helps the aggressive ions like  $\text{Cl}^-$  ions to diffuse on the coating surface. The Warburg reflects the semi-infinite length diffusion process, which results in the mass transfer process. The grain size and porosity affect the mass transport process very much. The as-sprayed coating has ~ 1.63 % porosity, which results in a  $207 \mu\text{cm}^2\Omega \text{ s}^{0.5}$  value of Warburg after 1 hr of immersion. The coating does not show the diffusion mechanism with a further increase in the immersion time (200 and 1000 hrs). In the case of the coatings annealed at 500 and 600 °C, the value of Warburg after 1 hr of immersion further decreased to 176.4 and  $159.76 \mu\text{cm}^2\Omega \text{ s}^{0.5}$ , respectively. The reduction in the value of Warburg is due to the increase in grain size after annealing. The maximum value of Warburg (~  $345.87 \mu\text{cm}^2\Omega \text{ s}^{0.5}$ ) was shown by the coating after annealing at 700 °C due to its fine grain size and minimum value of porosity. The EIS results were in support of the PDP

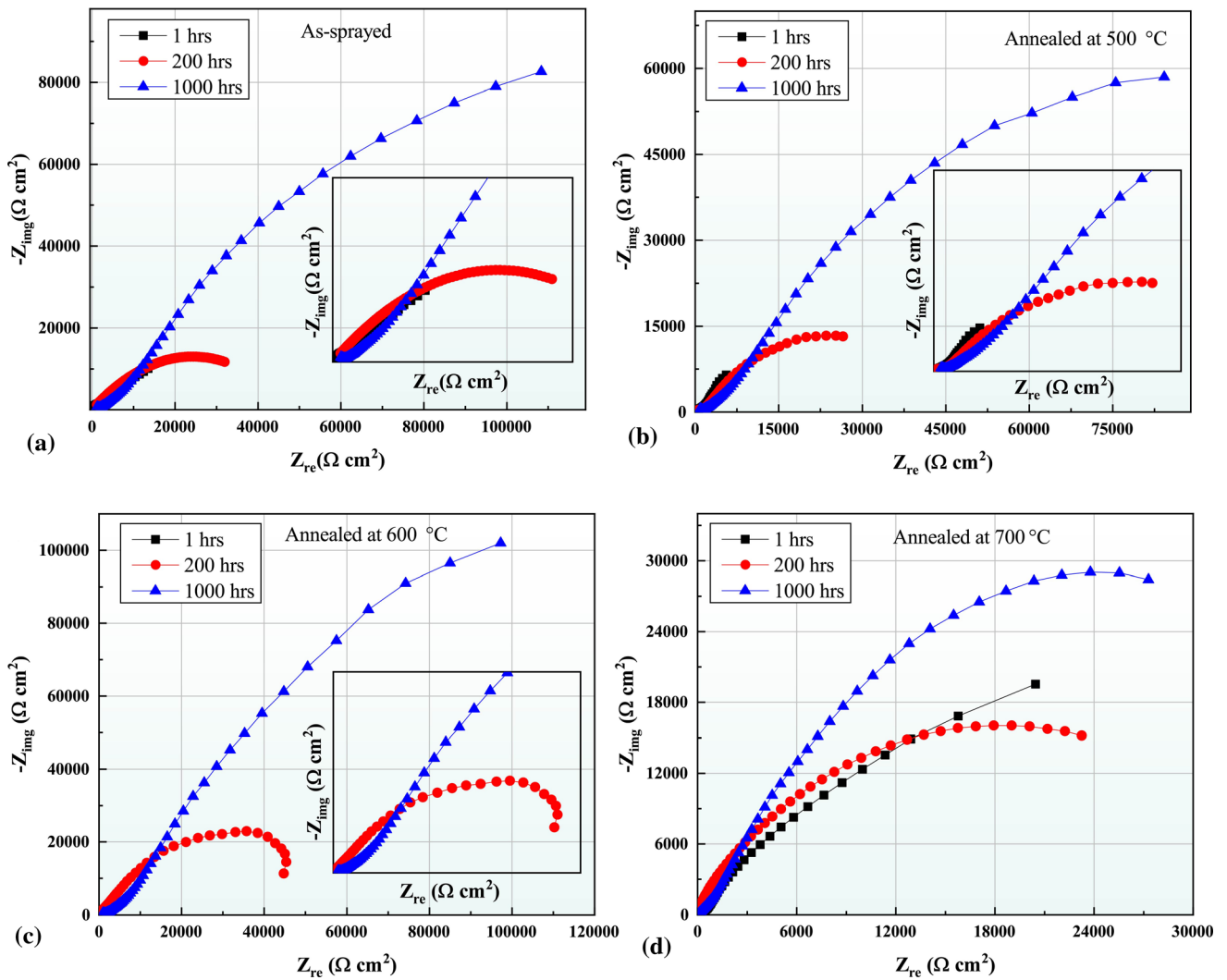


**Fig 5** Nyquist plots of all coating samples for different exposure periods: (a) as-sprayed, (b) annealed at 500 °C, (c) annealed at 600 °C, (d) annealed at 700 °C.

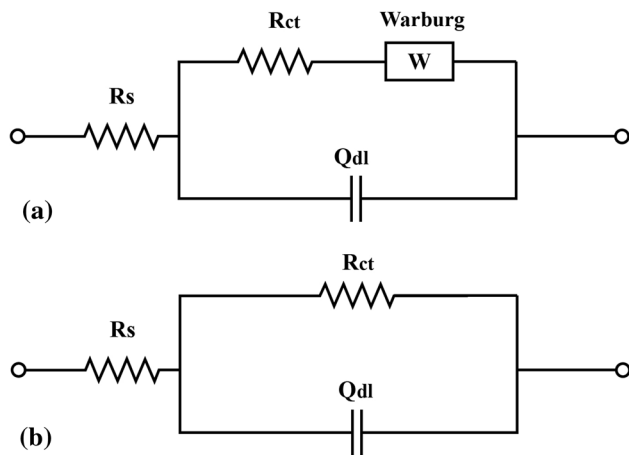


**Fig. 6** Equivalent circuit models for (a) all coatings after immersion for 1 hour, (b) all coatings after immersion for 200 and 1000 hours.

results, which also showed that coating shows the low dissolution of 0.43 mpy after annealing at 700 °C.

### Conclusion

The aluminum coatings were deposited on mild steel substrates by wire arc spraying and subsequently annealed at various temperatures. The annealing promoted the elemental interdiffusion and formation of oxides in the coatings. The grain size in the coatings increased gradually as the annealing temperature increased up to 600 °C and above that temperature, it decreased. After annealing at 500, 600 °C, the coatings exhibited inferior corrosion resistance which could be associated with their large grain size. The corrosion resistance of the coating was significantly improved after annealing at 700 °C. It could be



**Table 6** Impedance parameters obtained by fitting EEC models on all coatings with different immersion time

Sample ID	Immersion time, hrs	$R_s$ , $\Omega \text{ cm}^2$	$R_{ct}$ , $k\Omega \text{ cm}^2$	$Q_{dl}$ , $\mu\text{F/cm}^2$	$n_{dl}$	$W$ , $\mu\text{cm}^2 \Omega \text{ s}^{0.5}$
As-Sprayed	1	56.12	13.47	2.46	0.65	207.9
	200	117.54	17.03	3.57	0.64	....
	1000	176.43	408.51	4.88	0.41	....
Annealed at 500 °C	1	52.11	5.59	2.12	0.69	176.4
	200	114.21	11.87	3.06	0.44	....
	1000	170.12	410.23	4.12	0.54	....
Annealed at 600 °C	1	51.55	3.464	2.09	0.55	159.76
	200	112.87	14.99	3.11	0.65	....
	1000	169.45	389.2	4.29	0.47	....
Annealed at 700 °C	1	55.63	20.44	5.76	0.67	345.87
	200	119.88	33.46	6.19	0.77	....
	1000	180.32	511.76	6.89	0.53	....

concluded that various factors were responsible for the enhanced corrosion resistance, such as low porosity, the formation of corrosion resistant oxides, and smaller grain size.

## References

- V. Totolin, V. Pejaković, T. Csanyi, O. Hekele, M. Huber and M. Rodríguez Ripoll, Surface Engineering of Ti6Al4V Surfaces for Enhanced Tribocorrosion Performance in Artificial Seawater, *Mater. Des.*, 2016, **104**, p 10-18.
- H.S. Lee, J.K. Singh, M.A. Ismail, C. Bhattacharya, A.H. Seikh, N. Alharthi and R.R. Hussain, Corrosion Mechanism and Kinetics of Al-Zn Coating Deposited by Arc Thermal Spraying Process in Saline Solution at Prolong Exposure Periods, *Sci. Rep.*, 2019, **9**(1), p 1-17. <https://doi.org/10.1038/s41598-019-39943-3>
- S. Paswan, J.K. Singh and D.D.N. Singh, Effect of Lead Alloying on Corrosion Characteristics of Galvanized Coatings Exposed in Atmosphere, *Simul. Lab. Serv. Environ. Surf. Interf.*, 2020 <https://doi.org/10.1016/j.surfin.2020.100752>
- R. Sadeghi Erami, M. Amirnasr, S. Meghdadi, M. Talebian, H. Farrokhpour and K. Raeissi, Carboxamide Derivatives as New Corrosion Inhibitors for Mild Steel Protection in Hydrochloric Acid Solution, *Corros. Sci.*, 2019, **151**, p 190-197. <https://doi.org/10.1016/j.corsci.2019.02.019>
- K. Aoudia, S. Lamri, S. Achache, D. Retraint, C. Verdy, C. Langlade, S. Azem and F. Sanchette, Structural and Mechanical Properties of Arc-Sprayed Ni-Cr Coating Post-Treated by Surface Mechanical Attrition Treatment (SMAT), *Coatings*, 2018, **8**(12), p 12-17.
- K. Szymanski, A. Hernas, G. Moskal and H. Myalska, Thermally Sprayed Coatings Resistant to Erosion and Corrosion for Power Plant Boilers - A Review, *Surf. Coat. Tech.*, 2015, **268**, p 153-164. <https://doi.org/10.1016/j.surfcoat.2014.10.046>
- H.-S. Lee and J.K. Singh, Influence of Calcium Nitrate on Morphology and Corrosion Characteristics of Ammonium Phosphate Treated Aluminum Coating Deposited by Arc Thermal Spraying Process, *Corros. Sci.*, 2019, **146**, p 254-268. <https://doi.org/10.1016/j.corsci.2018.10.035>
- M.A. Ashraf, A. Salman, M.U. Manzoor and A. Farooq, Effect of Sol-Gel Sealing Method on the Corrosion Resistance of Plasma-Sprayed WC – 12 % Co Coatings, *Phys. Met. Metallogr.*, 2021, **122**(11), p 1088-1094.
- G. Bolelli, L.-M. Berger, T. Börner, H. Koivuluoto, V. Matikainen, L. Lusvarghi, C. Lyphout, N. Markocsan, P. Nylén, P. Sassatelli, R. Trache and P. Vuoristo, Sliding and Abrasive Wear Behaviour of HVOF- and HVOF-Sprayed Cr3C2–NiCr Hard-metal Coatings, *Wear*, 2016, **358-359**, p 32-50. <https://doi.org/10.1016/j.wear.2016.03.034>
- T.-C. Chen, C.-C. Chou, T.-Y. Yung, R.-F. Cai, J.-Y. Huang and Y.-C. Yang, A Comparative Study on the Tribological Behavior of Various Thermally Sprayed Inconel 625 Coatings in a Saline Solution and Deionized Water, *Surf. Coat. Tech.*, 2020 <https://doi.org/10.1016/j.surfcoat.2020.125442>
- S. Salavati, L. Pershin, T.W. Coyle and J. Mostaghimi, Effect of Porosity Content of Arc-Sprayed Alloy 625 Skins on the Flexural Behavior of Nickel Foam Core Sandwich Structures, *J. Therm. Spray Tech.*, 2014, **24**(1-2), p 215-221.
- S.F. Bonabi, F. Ashrafzadeh, A. Sanati and S.M. Nahvi, Structure and Corrosion Behavior of Arc-Sprayed Zn-Al Coatings on Ductile Iron Substrate, *J. Therm. Spray Tech.*, 2018, **27**(3), p 524-537. <https://doi.org/10.1007/s11666-018-0694-2>
- L. Pawlowski, *The Science and Engineering of Thermal Spray Coatings*, 2nd ed. Wiley, New Jersey, 2008.
- A. Darabi and F. Azarmi, Investigation on Relationship Between Microstructural Characteristics and Mechanical Properties of Wire-Arc-Sprayed Zn-Al Coating, *J. Therm. Spray Tech.*, 2020, **29**(1-2), p 297-307. <https://doi.org/10.1007/s11666-019-00919-4>
- I.C. Park and S.J. Kim, Corrosion Behavior in Seawater of Arc Thermal Sprayed Inconel 625 Coatings with Sealing Treatment, *Surf. Coat. Tech.*, 2017, **325**, p 729-737. <https://doi.org/10.1016/j.surfcoat.2017.03.009>
- H.S. Lee, J.K. Singh and J.H. Park, Pore Blocking Characteristics of Corrosion Products Formed on Aluminum Coating Produced by Arc Thermal Metal Spray Process in 3.5 Wt.% NaCl Solution, *Constr. Build. Mater.*, 2016, **113**, p 905-916. <https://doi.org/10.1016/j.conbuildmat.2016.03.135>
- H.S. Lee, J.K. Singh, M.A. Ismail and C. Bhattacharya, Corrosion Resistance Properties of Aluminum Coating Applied by Arc Thermal Metal Spray in SAE J2334 Solution with Exposure Periods, *Metals (Basel)*, 2016, **6**(3), p 55-69.
- S. Paul, S. Shrestha, C.M. Lee and M.D.F. Harvey, Thermally Sprayed Aluminium (TSA) Coatings for Extended Design Life of 22%Cr Duplex Stainless Steel in Marine Environments, *J. Therm. Spray Tech.*, 2013, **22**(2-3), p 328-336.

19. W. Zhao, T. Zhang, R. Xin, M. Wang, H. Ai, J. Sun and Y. Wang, Effects of Thermally Sprayed Aluminium Coating on the Corrosion Fatigue Behavior of X80 Steel in 3.5 Wt.% NaCl, *J. Therm. Spr. Tech.*, 2015, **24**(6), p 974-983.
20. C. Quoc Ly, Q. Le Thu, T. Van Nguyen, H. Thi To Phung and D. The Ngo, Heat Treatment of Thermal Spray Duplex Coating System of Aluminum-Nickel Chromium Alloy on Carbon Steel, *J. Therm. Spray. Tech.*, 2013, **22**(8), p 1383-1387.
21. W. Guo, Y. Wu, J. Zhang and W. Yuan, Effect of the Long-Term Heat Treatment on the Cyclic Oxidation Behavior of Fe-Based Amorphous/Nanocrystalline Coatings Prepared by High-Velocity Arc Spray Process, *Surf. Coat. Tech.*, 2016, **307**, p 392-398. <https://doi.org/10.1016/j.surfcoat.2016.09.018>
22. J. Lin, Z. Wang, P. Lin, J. Cheng, X. Zhang and S. Hong, Effects of Post Annealing on the Microstructure, Mechanical Properties and Cavitation Erosion Behavior of Arc-Sprayed FeNiCrB-SiNbW Coatings, *Mater. Des.*, 2015, **65**, p 1035-1040. <https://doi.org/10.1016/j.matdes.2014.10.066>
23. L. Janka, J. Norpoth, R. Trache and L.M. Berger, Influence of Heat Treatment on the Abrasive Wear Resistance of a Cr3C2NiCr Coating Deposited by an Ethene-Fuelled HVOF Spray Process, *Surf. Coat. Tech.*, 2016, **291**, p 444-451. <https://doi.org/10.1016/j.surfcoat.2016.02.066>
24. T. Kuranishi, H. Habazaki and H. Konno, Oxidation-Resistant Multilayer Coatings Using an Anodic Alumina Layer as a Diffusion Barrier on  $\gamma$ -TiAl Substrates, *Surf. Coat. Tech.*, 2005, **200**(7), p 2438-2444.
25. J. Zhou, M. Yang, R. Wang and X. Pang, Annealing Behavior of Aluminum Coating Prepared by Arc Spraying on P355NL1 Steel, *Surf. Coat. Tech.*, 2017, **330**, p 53-60. <https://doi.org/10.1016/j.surfcoat.2017.09.073>
26. N. Ahmed, M.A. Iqbal, Z.S. Khan and A.A. Qayyum, DC Magnetron-Sputtered Mo Thin Films with High Adhesion, Conductivity and Reflectance, *J. Electron. Mater.*, 2020, **49**(7), p 4221-4230. <https://doi.org/10.1007/s11664-020-08138-2>
27. M.K. Hedges, A.P. Newbery and P.S. Grant, Characterisation of Electric Arc Spray Formed Ni Superalloy IN718, *Mater. Sci. Eng. A*, 2002, **326**(1), p 79-91.
28. S. Kobayashi and T. Yakou, Control of Intermetallic Compound Layers at Interface between Steel and Aluminum by Diffusion-Treatment, *Mater. Sci. Eng. A*, 2002, **338**(1), p 44-53. [https://doi.org/10.1016/S0921-5093\(02\)00053-9](https://doi.org/10.1016/S0921-5093(02)00053-9)
29. Y. Tanaka and M. Kajihara, Kinetics of Isothermal Reactive Diffusion between Solid Fe and Liquid Al, *J. Mater. Sci.*, 2010, **45**(20), p 5676-5684. <https://doi.org/10.1007/s10853-010-4633-y>
30. T.C. Chen, C.C. Chou, T.Y. Yung, K.C. Tsai and J.Y. Huang, Wear Behavior of Thermally Sprayed Zn/15Al, Al and Inconel 625 Coatings on Carbon Steel, *Surf. Coat. Tech.*, 2016, **303**, p 78-85. <https://doi.org/10.1016/j.surfcoat.2016.03.095>
31. Y. Chen, X. Liang, S. Wei, Y. Liu and B. Xu, Heat Treatment Induced Intermetallic Phase Transition of Arc-Sprayed Coating Prepared by the Wires Combination of Aluminum-Cathode and Steel-Anode, *Appl. Surf. Sci.*, 2009, **255**(19), p 8299-8304. <https://doi.org/10.1016/j.apsusc.2009.05.142>
32. H.V. Pham, D. Maruoka and M. Nanko, Influences of Al<sub>2</sub>O<sub>3</sub> Grain Size on High-Temperature Oxidation of Nano-Ni/Al<sub>2</sub>O<sub>3</sub> Composites, *J. Asian Ceram. Soc.*, 2016, **4**(1), p 120-123. <https://doi.org/10.1016/j.jascer.2016.01.003>
33. Z. Chen and K. Yan, Grain Refinement of Commercially Pure Aluminum with Addition of Ti and Zr Elements Based on Crystallography Orientation, *Sci. Rep.*, 2020, **10**(1), p 1-8. <https://doi.org/10.1038/s41598-020-73799-2>
34. R.G. Kelly, J.R. Scully, D. Shoesmith and R.G. Buchheit, *Electrochemical Techniques in Corrosion Science and Engineering*, CRC Press, Florida, 2002.
35. B. Syrek-Gerstenkorn, S. Paul and A.J. Davenport, Sacrificial Thermally Sprayed Aluminium Coatings for Marine Environments: A Review, *Coatings*, 2020, **10**(3), p 267.
36. J. Chen, Y. Song, D. Shan and E.-H. Han, Modifications of the Hydrotalcite Film on AZ31 Mg Alloy by Phytic Acid: The Effects on Morphology, Composition and Corrosion Resistance, *Corros. Sci.*, 2013, **74**, p 130-138. <https://doi.org/10.1016/j.corsci.2013.04.034>
37. T.Y. Yung, T.C. Chen, K.C. Tsai, W.F. Lu, J.Y. Huang and T.Y. Liu, Thermal Spray Coatings of Al, ZnAl and Inconel 625 Alloys on SS304L for Anti-Saline Corrosion, *Coatings*, 2019, **9**(1), p 32.
38. F. Mansfeld, "Electrochemical Methods of Corrosion Testing," Corrosion: Fundamentals, Testing, and Protection, S.D. Cramer and B.S. Covino Jr., Eds., ASM International, 2003, <https://doi.org/10.31399/asm.hb.v13a.a0003644>.
39. S. Saeidi, K.T. Voisey and D.G. McCartney, The Effect of Heat Treatment on the Oxidation Behavior of HVOF and VPS CoNiCrAlY Coatings, *J. Therm. Spray Technol.*, 2009, **18**(2), p 209-216.
40. S.G. Wang, M. Sun, H.B. Han, K. Long and Z.D. Zhang, The High-Temperature Oxidation of Bulk Nanocrystalline 304 Stainless Steel in Air, *Corros. Sci.*, 2013, **72**, p 64-72. <https://doi.org/10.1016/j.corsci.2013.03.008>
41. C. Chen, C. Lu, X. Feng and Y. Shen, Effects of Annealing on Al-Si Coating Synthesised by Mechanical Alloying, *Surf. Eng.*, 2017, **33**(7), p 548-558. <https://doi.org/10.1080/02670844.2017.1292706>
42. K.M. Deen, M. Afzal, Y. Liu, A. Farooq, A. Ahmad and E. Asselin, Improved Corrosion Resistance of Air Plasma Sprayed WC-12%Co Cermet Coating by Laser Re-Melting Process, *Mater. Lett.*, 2017, **191**, p 34-37. <https://doi.org/10.1016/j.matlet.2017.01.010>
43. B.-Y. Chang, Conversion of a Constant Phase Element to an Equivalent Capacitor, *J. Electrochem. Sci. Tech.*, 2020, **11**(3), p 318-321.
44. B.J. Wang, D.K. Xu, Y.C. Xin, L.Y. Sheng and E.H. Han, High Corrosion Resistance and Weak Corrosion Anisotropy of an As-Rolled Mg-3Al-1Zn (in wt.%) Alloy with Strong Crystallographic Texture, *Sci. Rep.*, 2017, **7**(1), p 16014. <https://doi.org/10.1038/s41598-017-16351-z>
45. J.J. Gray and C.A. Orme, Electrochemical Impedance Spectroscopy Study of the Passive Films of Alloy 22 in Low PH Nitrate and Chloride Environments, *Electrochim. Acta*, 2007, **52**(7), p 2370-2375. <https://doi.org/10.1016/j.electacta.2006.08.043>
46. E. Abedi Esfahani, H. Salimijazi, M.A. Golozar, J. Mostaghimi and L. Pershin, Study of Corrosion Behavior of Arc Sprayed Aluminum Coating on Mild Steel, *J. Therm. Spray Tech.*, 2012, **21**(6), p 1195-1202.

**Publisher's Note** Springer Nature remains neutral with regard to jurisdictional claims in published maps and institutional affiliations.